computation

MDPI

*Article*

# A Method for Road Spectrum Identification in Real-Vehicle Tests by Fusing Time-Frequency Domain Features

**Biao Qiu and Chaiyan Jettanasen ***

School of Engineering, King Mongkut's Institute of Technology Ladkrabang, Bangkok 10520, Thailand; 63601010@kmitl.ac.th

* Correspondence: chaiyan.je@kmitl.ac.th

**Abstract**

Most unpaved roads are subjectively classified as Class D roads. However, significant variations exist across different sites and environments (e.g., mining areas). A major challenge in the engineering field is how to quickly correct the Power Spectral Density (PSD) of the unpaved road in question using existing equipment and limited sensors. To address this issue, this study combines real-vehicle test data with a suspension dynamics simulation model. It employs time-domain reconstruction via Inverse Fast Fourier Transform (IFFT) and wavelet processing methods to construct an optimized model that fuses time-frequency domain features. With the help of a surrogate optimization method, the model achieves the best approximation of the actual road surface, corrects the PSD parameters of the unpaved road, and provides a reliable input basis for vehicle dynamics simulation, fatigue life prediction, and performance evaluation.

**Keywords:** power spectral density (PSD); inverse fast Fourier transform (IFFT); time-frequency domain fusion; unpaved road; surrogate optimization

Check for updates

Academic Editor: Andry Sedelnikov

Received: 5 December 2025
Revised: 14 January 2026
Accepted: 19 January 2026
Published: 2 February 2026

**Copyright:** © 2026 by the authors. Licensee MDPI, Basel, Switzerland. This article is an open access article distributed under the terms and conditions of the Creative Commons Attribution (CC BY) license.

## 1. Introduction

The Road Power Spectral Density (PSD) is a core indicator for characterizing the statistical properties of road roughness, and serves as a critical input for vehicle dynamics simulation, fatigue life prediction, and driving performance evaluation. Road spectrum identification refers to the technical process of obtaining this indicator either by calculating through direct measurement of road contours or by inverting based on vehicle vibration responses [1–3]. This identification is particularly important for off-highway vehicles with special structures (e.g., mining trucks), which often operate on unpaved roads such as dirt roads and gravel roads. The road spectrum characteristics of these roads vary significantly depending on specific sites and environments, yet they were traditionally and subjectively classified uniformly as Class D roads [4,5]. This simplistic handling method fails to accurately reflect the diversity of actual road conditions, leading to deviations between simulation results and engineering practice. Therefore, conducting research on road spectrum identification of unpaved roads plays a vital role in the design and driving safety of off-highway vehicles.

Road spectrum identification is categorized into direct measurement methods and indirect identification methods. Direct measurement methods require significant labor and costs, which largely limit their practical application [6]. Therefore, scholars have conducted extensive research on indirect identification methods for road spectrum. Based on core technical principles and modeling logic, indirect road spectrum identification methods

can be divided into three categories: state estimation methods based on physical models, mapping learning methods based on data-driven approaches, and feature analysis methods based on signal processing [7].

The core principle of the state estimation method based on physical models is to construct vehicle dynamics equations and infer road input parameters through state estimation algorithms. The main estimation algorithms for road excitation inversion include the Kalman Filter (KF) algorithm [8], the Unscented Kalman Filter (UKF) algorithm [9], and the Extended Kalman Filter (EKF) algorithm [10]. Among these, EKF and UKF are designed to address estimation problems for nonlinear vehicle models (e.g., mining trucks equipped with hydro-pneumatic suspension). To achieve high-precision and high-robustness inference of road roughness, in addition to KF-series algorithms, scholars have also applied various estimation methods such as the $H_2$ observer [11], the second-order sliding mode observer [12], and the regularized least squares method [2].

The data-driven mapping learning method does not rely on complex physical models. Instead, it enables algorithms to learn the mapping relationship between vehicle response and road spectrum from the vehicle response data corresponding to known roads. Furthermore, based on the trained mapping relationship model, it realizes the inversion of road roughness. In recent years, with the maturity of machine learning and deep learning technologies, such data-driven methods have been widely applied in road feature identification. Common algorithms include Support Vector Machine (SVM) [13], Random Forest (RF) [14], Convolutional Neural Network (CNN) [15], Long Short-Term Memory (LSTM) [16], and hybrid neural network (CNN-LSTM) [17]. In practical applications, the selection of algorithms often requires comprehensive trade-offs based on data scale, feature complexity, and real-time requirements.

The feature analysis method based on signal processing treats vehicle dynamic responses as time-varying signals. It uses signal processing techniques such as the Fourier transform and wavelet transform to extract robust features, and then explores the intrinsic correlation between these features and road parameters to achieve the inversion of road roughness. Its technical path mainly centers on the dimensional transformation of signals, which includes three aspects: first, time-domain analysis directly targeting signal waveforms [18]; second, frequency-domain analysis focusing on frequency composition [19]; and third, time-frequency analysis that balances time and frequency resolution [20]. Specifically, the time-domain analysis path is suitable for evaluating the roughness level of stable and uniform roads and identifying local defects; the frequency-domain analysis path is suitable for inverting the roughness PSD of stable and uniform roads and classifying road types; and the time-frequency joint analysis path is suitable for the dynamic identification of non-stationary mixed roads (e.g., mining area roads) and the monitoring of sudden changes in road conditions.

Although significant progress has been made in road spectrum identification methods both in theory and application, existing studies still have certain limitations. First, while the state estimation method based on physical models has a clear dynamic mechanism, it has high requirements for model accuracy and parameter sensitivity—especially in nonlinear suspension systems (e.g., hydro-pneumatic suspension), where estimation deviations are prone to occur. In addition, although data-driven methods can avoid complex modeling, their generalization ability is limited by the coverage of training data, making it difficult to adapt to variable road conditions. More critically, most existing methods focus on feature extraction in a single domain (either time domain or frequency domain) and fail to fully leverage the representational advantages of time-frequency joint features under non-stationary and non-uniform road conditions. This results in shortcomings in the authenticity and robustness of the inverted road PSD. In contrast, the PSD identification

method proposed in this paper integrates time-domain reconstruction and frequency-domain analysis techniques. By constructing a multi-feature joint optimization objective, it can more comprehensively and accurately approximate the statistical characteristics of actual roads, and is particularly suitable for complex scenarios with strong non-stationary characteristics such as unpaved roads.

The accurate identification of frequency components of road PSD plays a core supporting role in optimizing vehicle ride comfort and protecting driver health, stemming from the significant frequency dependence of human sensitivity to vibration. According to the ISO 2631 standard [21] and relevant research [22], low-frequency vibrations (<5 Hz) tend to induce resonance of human visceral organs, leading to discomfort symptoms such as fatigue and nausea. In contrast, mid-frequency vibrations (5–20 Hz) mainly affect the musculoskeletal system, and long-term exposure may increase the risk of low back injuries. These two frequency bands are exactly the main concentration areas of vibration energy on unpaved roads. The accurate identification of their frequency components is of crucial guiding significance for the optimization of vehicle suspension systems and the design of vibration attenuation structures. Traditional single-domain feature extraction methods struggle to accurately capture the frequency distribution details of such non-stationary vibrations, especially the energy proportion and dynamic variation law of low- and mid-frequency bands. The time-frequency domain feature fusion method proposed in this paper, which combines the Inverse Fast Fourier Transform (IFFT) with wavelet analysis, can accurately characterize the characteristics of key frequency bands, thereby providing reliable support for performance optimization related to vehicle ride comfort and driver health protection.

To address the aforementioned issues, this study focuses on the efficient and high-precision identification of the PSD for unpaved roads. First, based on the sprung/unsprung mass acceleration data obtained from real-vehicle tests, a quarter-vehicle simulation system is constructed by integrating a nonlinear dynamic model of the hydro-pneumatic suspension system. Subsequently, the IFFT is employed to reconstruct the time-domain road excitation, and wavelet analysis is used to perform time-frequency domain decomposition and reconstruction of the measured signals, thereby extracting robust time-frequency domain feature quantities. On this basis, a multi-objective optimization model targeting the minimization of feature errors between simulation and experiment is established, and a surrogate optimization algorithm is introduced to efficiently solve for the road PSD parameters ($Ge$, $Gs$, $Ga$). This method enables the full-process identification of road spectrum parameters from measured data, featuring both a clear mechanism and high computational efficiency. It provides a reliable input basis for the dynamic simulation and performance evaluation of off-highway vehicles under real operating conditions. The technical route framework of this study is shown in Figure 1.

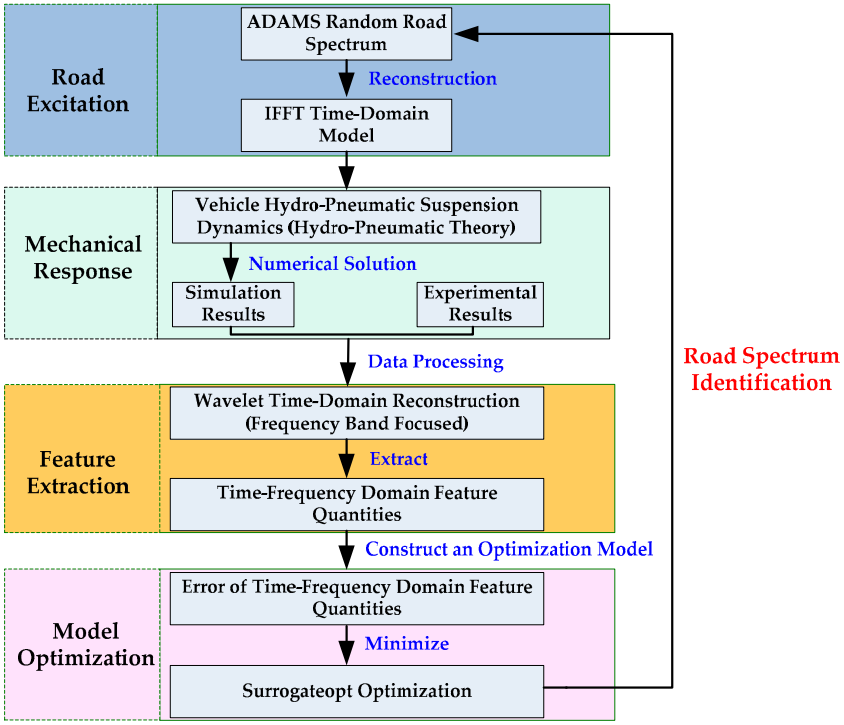



**Figure 1.** Framework of the technical route.

## 2. Mathematical Model

To clarify the physical variables involved in the subsequent model derivation, Table 1 lists the symbols, physical meanings, and corresponding units of all variables in this section.

**Table 1.** Definition and units of variables.

| Symbol | Physical Meaning | Unit | Symbol | Physical Meaning | Unit |
|---|---|---|---|---|---|
| $m_1$ | Unsprung mass | kg | $V_0$ | Initial gas volume | $m^3$ |
| $m_2$ | Sprung mass | kg | $V_1$ | Gas volume at an arbitrary state | $m^3$ |
| $x_g$ | Random road displacement | m | $P_{g0}$ | Initial gas pressure | MPa |
| $x_1$ | Unsprung mass displacement | m | $P_{g1}$ | Gas pressure at an arbitrary state | MPa |
| $x_2$ | Sprung mass displacement | m | $r$ | Gas polytropic exponent | - |
| $\ddot{x}_1$ | Unsprung mass acceleration | $m/s^2$ | $\Delta P$ | Pressure difference between Chamber I and Chamber II | MPa |
| $\ddot{x}_2$ | Sprung mass acceleration | $m/s^2$ | $q$ | Flow rate | $m^3/s$ |
| $\dot{x}_1$ | Unsprung mass velocity | m/s | $C_d$ | Flow coefficient | - |
| $\dot{x}_g$ | Velocity excitation of uneven road | m/s | $A_0$ | Cross-sectional area of the throttle orifice | $m^2$ |
| $k_1$ | Tire stiffness | kN/m | $\rho$ | Oil density | $kg/m^3$ |
| $c_1$ | Tire damping coefficient | kN·s/m | $A_{01}$ | Effective cross-sectional area of the constantly open damping orifice | $m^2$ |

**Table 1.** *Cont.*

| Symbol | Physical Meaning | Unit | Symbol | Physical Meaning | Unit |
|---|---|---|---|---|---|
| $A_1$ | Effective cross-sectional area of Chamber I | $m^2$ | $A_{02}$ | Effective cross-sectional area of the check valve | $m^2$ |
| $A_2$ | Effective cross-sectional area of Chamber II | $m^2$ | $d_{01}$ | Equivalent diameter of the constantly open damping orifice | m |
| $P_{s0}$ | Chamber pressure at the static equilibrium position | MPa | $d_{02}$ | Equivalent diameter of the check valve | m |
| $P_1$ | Pressure of Chamber I | MPa | $z$ | Relative displacement between the piston rod and cylinder barrel | m |
| $P_2$ | Pressure of Chamber II | MPa | $\dot{z}$ | Relative velocity between the piston rod and cylinder barrel | m/s |

### *2.1. Quarter-Vehicle Model with Hydro-Pneumatic Suspension*

The research object of this study is a mining truck equipped with a hybrid hydro-pneumatic suspension (HPS), and its quarter-vehicle model is shown in Figure 2a. All parameters involved in the model are defined in Table 1.

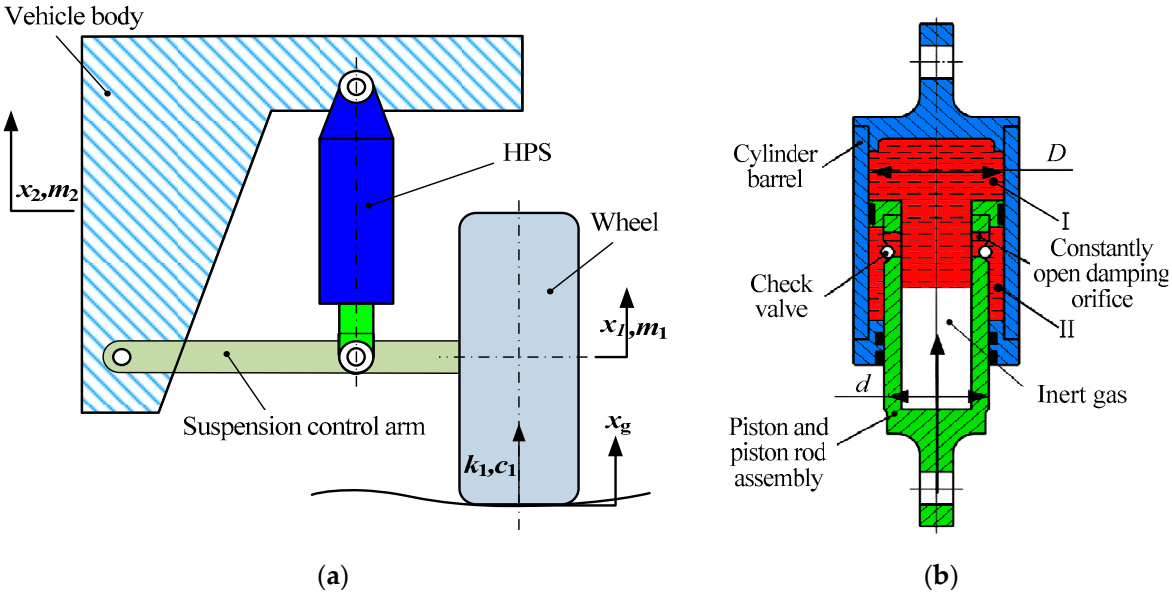



**Figure 2.** Quarter-vehicle model and its suspension structure. (**a**) Quarter-vehicle model with hybrid HPS, (**b**) schematic of the hybrid HPS.

Figure 2b shows a simplified structural diagram of the hybrid HPS, which is mainly composed of a cylinder barrel, a piston rod, and a piston assembly. There are two chambers inside the suspension cylinder, designated as Chamber I and Chamber II, respectively. The wall of the piston rod is provided with a damping orifice and a one-way valve orifice. The upper part of Chamber I and the entire Chamber II of the HPS are filled with hydraulic oil, while the lower part of Chamber I is filled with inert gas. Here, D represents the inner diameter of the cylinder barrel, and d represents the outer diameter of the piston rod. The inert gas acts as an elastic element, while the hydraulic oil in the suspension cylinder serves three functions: energy transmission, energy transfer, energy control, and additional lubrication. Due to the compressibility of the high-pressure nitrogen gas inside the suspension cylinder, the relative movement between the piston rod and the cylinder

barrel causes changes in the gas volume, thereby absorbing and releasing energy. During the compression stroke of the suspension hydraulic cylinder, the one-way valve opens, the volume of the annular chamber inside the cylinder increases, and the hydraulic oil flows from Chamber I to Chamber II through the fixed damping orifice and the one-way valve orifice. The damping force encountered during this movement is relatively small, and the gas in the air chamber is compressed to absorb energy. During the extension stroke of the suspension hydraulic cylinder, the one-way valve orifice closes, the volume of the annular chamber decreases, and the hydraulic oil flows only from Chamber II to Chamber I through the damping orifice. The damping force during this movement is relatively large, and the gas in the air chamber expands to release energy. It can be concluded that the fixed damping orifice of the piston rod and the effective flow area of the one-way valve in the suspension hydraulic cylinder directly affect the working characteristics of the suspension cylinder. Together with the cross-sectional area of the rodless chamber and the cross-sectional area of the rod chamber of the hydraulic cylinder, these parameters determine the vibration-damping performance of the entire HPS system.

To simplify the analysis, this study regards the tire as a linear stiffness element, which is a general assumption adopted in vehicle dynamics modeling for road surface spectrum identification [23]. However, it should be noted that tire load variations (e.g., load fluctuations during the loading and unloading operations of mining dump trucks) will affect the tire stiffness characteristics and thereby alter the transmission law of road excitation [24]. This study focuses on the core issue of road surface spectrum identification under the constant-speed and constant-load condition (a typical working condition during the transportation phase of mining dump trucks), where the linear stiffness assumption can meet the accuracy requirements for the identification of road PSD parameters. According to Newton's second law, the dynamic equations of the quarter-vehicle model can be obtained as follows:

$$m_1\ddot{x}_1 = -k_1(x_1 - x_g) - c_1(\dot{x}_1 - \dot{x}_g) - F - m_1 g \quad (1)$$

$$m_2\ddot{x}_2 = F - m_2 g \quad (2)$$

All variables in Equations (1) and (2) are defined in Table 1, where $F$ denotes the force of the HPS (the detailed calculation is given in Section 2.2).

### *2.2. Mathematical Model for Force Analysis of the HPS*

Based on the simplified structural diagram of the HPS shown in Figure 2, let $z$ and $\dot{z}$ represent the relative displacement and relative velocity between the piston rod and the cylinder barrel (or the displacement and velocity of the hydro-pneumatic strut), respectively. The extension direction is defined as positive to ensure consistency with the sign convention in the quarter-vehicle model. Drawing on the research experience of simplified hydraulic shock absorbers, the following assumptions are made when calculating the nonlinear force generated by the HPS [25]: ① It is assumed that there is no leakage between the piston, piston rod, and cylinder barrel. ② It is assumed that the HPS has good heat dissipation; the influence of temperature on the resistance characteristics is not considered, and the hydraulic oil temperature is regarded as constant throughout the extension and compression working processes. ③ The compressibility of the hydraulic oil is neglected, and the bulk modulus of the hydraulic oil is assumed to be constant. ④ The elastic deformation of the rigid components of the system caused by pressure changes is neglected. ⑤ The gravitational potential energy of the working hydraulic oil is ignored. ⑥ The instantaneous pressure is uniform everywhere in the same chamber.

The effective cross-sectional areas of the two chambers (Chamber I and Chamber II) are as follows:

$$\left.\begin{array}{l} A_1 = \frac{\pi}{4}D^2 \\ A_2 = \frac{\pi}{4}\left(D^2 - d^2\right) \end{array}\right\} \tag{3}$$

Under static equilibrium, we have the following:

$$m_2 g = P_{s0}(A_1 - A_2) = \frac{\pi}{4}P_{s0}d^2 \tag{4}$$

(1) Force equation of the entire chamber. Taking the oil cylinder as the research object, we can obtain the following:

$$F = P_1 A_1 - P_2 A_2 \tag{5}$$

(2) The gas in the air chamber of the HPS is nitrogen, whose properties are similar to those of an ideal gas. Its state change process can be expressed as follows:

$$P_{g1}V_1^r = P_{g0}V_0^r \tag{6}$$

where variables $V_0$, $V_1$, $\boldsymbol{P_{g0}}$, $\boldsymbol{P_{g1}}$ refer to Table 1; $r$ denotes the gas polytropic exponent. During rapid loading, the gas undergoes an adiabatic process, where $\boldsymbol{r = 1.4}$; during slow loading, the gas undergoes an isothermal process, where $\boldsymbol{r = 1}$. In practical scenarios, dump trucks experience road jolts, and the suspension is mostly subject to rapid loading, so the gas polytropic exponent is usually taken as $\boldsymbol{r = 1.4}$.

(3) The pressure difference between Chamber I and Chamber II is expressed as follows:

$$\Delta P = P_1 - P_2 \tag{7}$$

where $\boldsymbol{\Delta P}$ is generated by the damping of the damping orifice and one-way valve of the suspension cylinder.

(4) For the mathematical model of the orifice, according to the throttling theory of liquid passing through a thin-walled orifice [26], we can obtain the following:

$$\Delta P = \frac{1}{2}\rho\left(\frac{q}{C_d A_0}\right)^2 \tag{8}$$

For the damping orifice with a one-way valve, we can obtain the following:

$$A_0 = A_{01} + 0.5A_{02}\left(1 - \mathrm{sign}\left(\dot{z}\right)\right) \tag{9}$$

where $\boldsymbol{A_{01} = \pi/4d_{01}^2}$, $\boldsymbol{A_{02} = \pi/4d_{02}^2}$; sign(·) denotes the signum function.

Substituting Equation (9) into Equation (8), we can obtain the following:

$$\Delta P = \frac{1}{2}\rho\left(\frac{q}{C_d\left(A_{01} + 0.5A_{02}\left(1 - \mathrm{sign}\left(\dot{z}\right)\right)\right)}\right)^2 \tag{10}$$

When the hydro-pneumatic strut is in a compressed state, the one-way valve opens; otherwise, the one-way valve closes. When the flow rate is constant, an increase in $\boldsymbol{A_0}$ will cause the pressure difference $\boldsymbol{\Delta P}$ to decrease, and the resulting damping force will also decrease accordingly.

(5) Calculation of flow rate $\boldsymbol{q}$. When the piston rod moves upward by $z$ relative to the piston cylinder, the increase in the liquid volume of Chamber II is $\boldsymbol{\Delta V_2 = A_2 z}$ Taking the derivative of both sides with respect to time, we obtain the following:

$$q = A_2\dot{z} \tag{11}$$

(6) The force on the entire chamber can be written as follows:

$$F = P_1 A_1 - (P_1 - \Delta P)A_2 = P_1(A_1 - A_2) + \Delta P A_2 = F_k - F_d \tag{12}$$

Combining Equation (6) and Equation (10), Equation (12) can be written as follows:

$$F = \frac{P_{g0} V_0^r (A_1 - A_2)}{(V_0 + (A_1 - A_2) \cdot z)^r} - \frac{1}{2}\rho \left( \frac{A_2 \dot{z}}{C_d \left( A_{01} + 0.5 A_{02} \left( 1 - \text{sign}(\dot{z}) \right) \right)} \right)^2 A_2 \text{sign}(\dot{z}) \tag{13}$$

It can be seen that the total force acting on the entire hydro-pneumatic strut consists of the elastic force $\boldsymbol{F_k}$ generated by the gas and the damping force $\boldsymbol{F_d}$ generated by the hydraulic oil.

### *2.3. Road Surface Time-Domain Modeling Based on the IFFT Method*

The road surface serves as the primary excitation source for vehicle systems, and road surface models form the foundation for full-vehicle simulations—particularly for analyzing vehicle ride comfort, handling stability, durability, and component load. The random linear vibration theory constructed based on road surface PSD and transfer functions is not applicable to vehicle dynamic models with nonlinear HPS; such nonlinear dynamic models require solutions using time-domain difference methods. Currently, the main methods for time-domain modeling of road surface irregularities include: the harmonic superposition method, the filtered white noise method, the AutoRegressive Moving Average (ARMA) model method, the Poisson method, and the IFFT method. The IFFT method exhibits efficient and accurate reconstruction capabilities, making it highly suitable for establishing road surface time-domain models [27,28]. It should be noted that the fundamental frequency of the engine is relatively high, and its impact on the results is minimal after filtering; therefore, the influence of engine excitation is neglected in the simulation.

The International Organization for Standardization (ISO) recommends that the statistical characteristics of road surface irregularities be represented by the PSD [29], and its spatial frequency PSD can be expressed as follows:

$$G_q(n) = G_q(n_0) \left( \frac{n}{n_0} \right)^{-2} \tag{14}$$

where $\boldsymbol{n}$ represents the spatial frequency, $\boldsymbol{G_q(n_0)}$ denotes the irregularity index, and $\boldsymbol{n_0}$ stands for the spatial reference frequency.

The parameters in the expression of Equation (14) mainly depend on the road surface irregularity index $\boldsymbol{G_q(n_0)}$, making it more suitable for paved roads. To further characterize the statistical properties of road surface irregularities for unpaved roads, ADAMS (Automatic Dynamic Analysis of Mechanical Systems) uses 3 parameters—$\boldsymbol{G_a}$, $\boldsymbol{G_s}$, and $\boldsymbol{G_e}$—to describe the statistical characteristics of random road surfaces. These parameters can simultaneously reflect the energy distribution at the levels of displacement, gradient, and curvature, and are more consistent with real-world road conditions (especially when the attenuation rates at low and high frequencies differ) [30]. Its expression is as follows:

$$G_q(n) = G_e + \frac{G_s}{(2\pi n)^2} + \frac{G_a}{(2\pi n)^4} \tag{15}$$

where the amplitude of the first term is $\boldsymbol{G_e}$, which is a white noise elevation term; the amplitude of the second term is $\boldsymbol{G_s}$, which is a white noise gradient (or equivalent velocity) term and requires one integration with respect to time; the amplitude of the third term is $\boldsymbol{G_a}$, which is a white noise acceleration term and requires two integrations with respect to

time. In this regard, the differences between different random road surfaces depend on $G_e$, $G_s$, and $G_a$.

Based on the relationship between spatial frequency and temporal frequency, the expression of the road PSD under temporal frequency is obtained as follows:

$$G_q(f) = G_e + \frac{v^2 G_s}{(2\pi f)^2} + \frac{v^4 G_a}{(2\pi f)^4} \tag{16}$$

where $v$ denotes the vehicle traveling speed, and $f$ represents the temporal frequency.

Based on the relationship between the PSD and the amplitude spectrum, $G_q(f)$ can be expressed as follows:

$$G_q(f) = \frac{2}{T}\left|X_g(f)\right|^2 = \frac{2}{T}\left|\int_0^T x_g(t)e^{-j2\pi ft}dt\right|^2 \tag{17}$$

where $X_g(f)$ denotes the amplitude spectrum of road surface irregularities, $x_g(t)$ represents the displacement of road surface irregularities over time, and $T$ stands for the total sampling time.

The phase spectrum can be regarded as a uniformly random distribution within the range of [0, 2π]. According to Equation (17), the amplitude spectrum is obtained through discrete sampling calculation, and then the time-dependent variation relationship of road surface irregularities can be acquired via IFFT. Under the condition of a vehicle speed of 20 km/h, the time-domain curves of road surface irregularities for China's national standard road classes C and D are shown in Figure 3. It can be verified that the root mean square (RMS) values of the road surface irregularity displacements at this time are 0.015 m and 0.0301 m, respectively, which are consistent with the results of the national standard [31]. This proves the reliability of time-domain modeling based on the IFFT method.

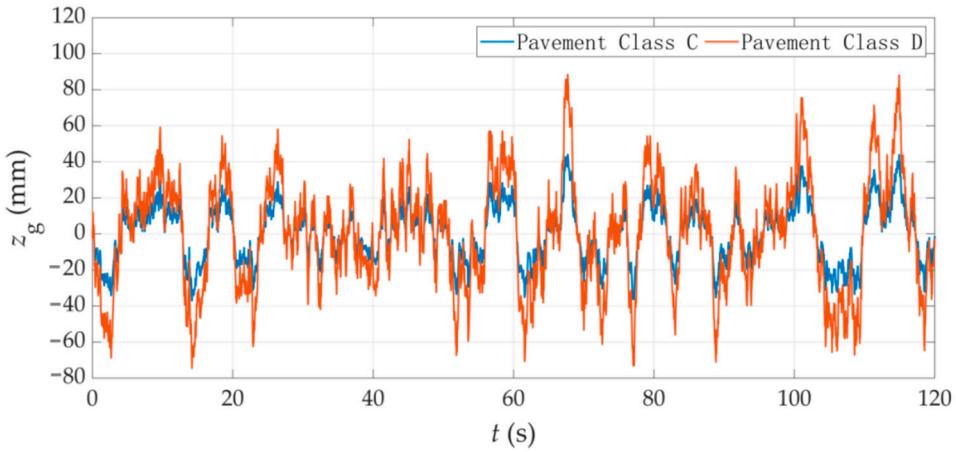



**Figure 3.** Road surface irregularity displacements of China national standard road Classes C and D at a vehicle speed of 20 km/h.

By the same token, the time-domain curves of irregularities for ADAMS' rough asphalt pavement and rough cement pavement at a vehicle speed of 20 km/h can be obtained, as shown in Figure 4.

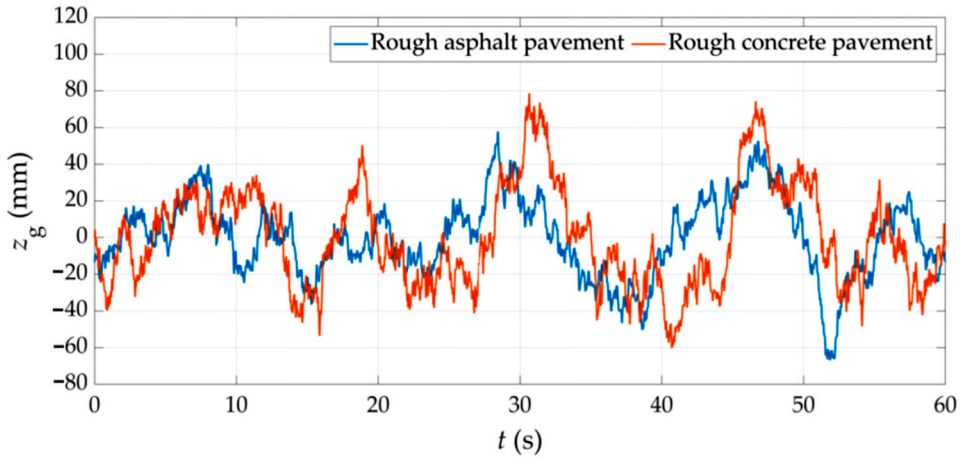



**Figure 4.** Road surface irregularity displacements of ADAMS' rough asphalt pavement and rough cement pavement at a vehicle speed of 20 km/h.

## 3. Simulation of Random Road Surface Suspension System

Based on material parameters, structural parameters, installation parameters, and bench test data, the model parameters of a quarter -vehicle with nonlinear HPS for a mining dump truck were obtained, as shown in Table 2. Among these parameters, the road spectrum values of the rough rigid cement road in ADAMS are $\boldsymbol{G_e = 0.1\ (m^3/cycle \times 10^{-6})}$, $\boldsymbol{G_s = 35\ (m/cycle \times 10^{-6})}$, and $\boldsymbol{G_a = 0.3\ (1/(m{\cdot}cycle) \times 10^{-6})}$ [32]. The simulation results of the quarter -vehicle on the random rough rigid cement road in ADAMS can be easily obtained, as shown in Figures 5 and 6.

**Table 2.** Parameters of quarter-vehicle dynamic simulation.

| Name | Symbol | Value | Unit | Name | Symbol | Value | Unit |
|---|---|---|---|---|---|---|---|
| Vehicle Speed | $v$ | 20 | km/h | Check Valve Diameter | $d_{02}$ | 10 | mm |
| Unsprung Mass | $m_1$ | 2000 | kg | Hydraulic Oil Density | $\rho$ | 860 | kg/m$^3$ |
| Tire Stiffness | $k_t$ | 1400 | kN/m | Cylinder Bore Diameter | $D$ | 190 | mm |
| Sprung Mass | $m_2$ | 8800 | kg | Piston Rod Outer Diameter | $d$ | 150 | mm |
| Gas Polytropic Exponent | $r$ | 1.4 | --- | Charging Pressure | $P_1$ | 4.85 | MPa |
| Damping Orifice Diameter | $d_{01}$ | 8 | mm | Charging Volume | $V_1$ | 1.25 | L |

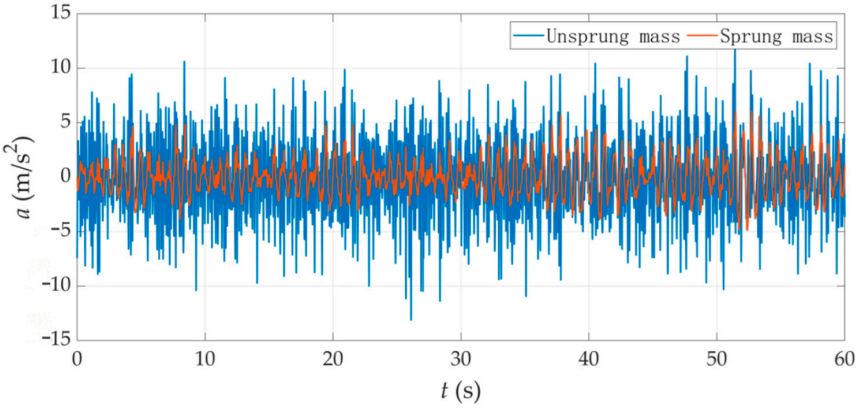



**Figure 5.** Time-domain acceleration responses of unsprung mass and sprung mass.

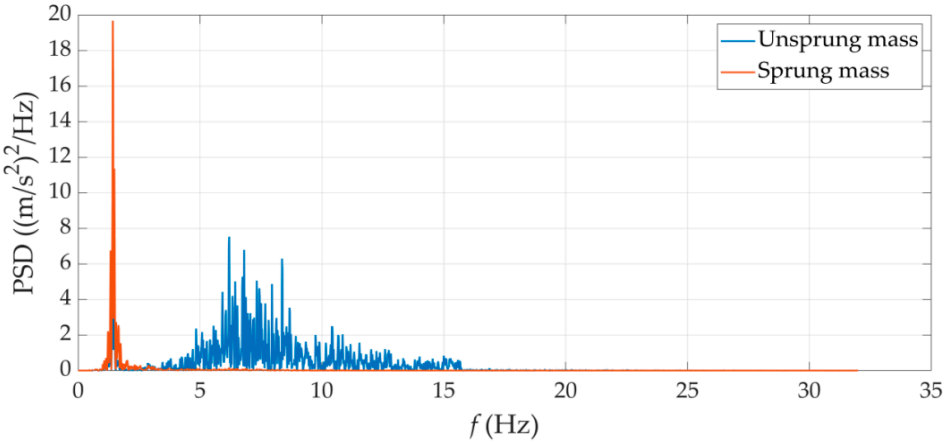



**Figure 6.** Frequency-domain acceleration responses of unsprung mass and sprung mass.

## 4. Experiments and Data Processing

### *4.1. Vibration Test of Mining Dump Truck*

At the test site, a vibration test was conducted on the mining dump truck to obtain the accelerations of the sprung mass and unsprung mass. Figure 7 shows the vibration test scheme and its layout, while Figure 8 presents the vehicle and equipment used in the test. The main test and analysis instruments include the German M + P signal acquisition and analysis system, PCB vibration sensors, and SO Analyzer 4.0 software. The measuring points of the acceleration sensors are arranged at the upper and lower ends of the HPS to measure the acceleration responses of the sprung mass and unsprung mass, respectively. During the experiment, the sampling frequency was set to 512 Hz, and the vehicle traveled at a constant speed of 20 km/h on the road to measure the accelerations of the unsprung mass and sprung mass. Considering the poor display effect of SO Analyzer, the experimental data were exported to MATLAB R2022a for further visualization, as shown in Figure 9. This figure depicts the acceleration responses of the sprung mass and unsprung mass when the vehicle is traveling at 20 km/h. Assuming that the road conditions between the left and right wheels, as well as the front and rear wheels of the vehicle, are approximately the same, the vehicle can be approximately simplified as a quarter-vehicle model.

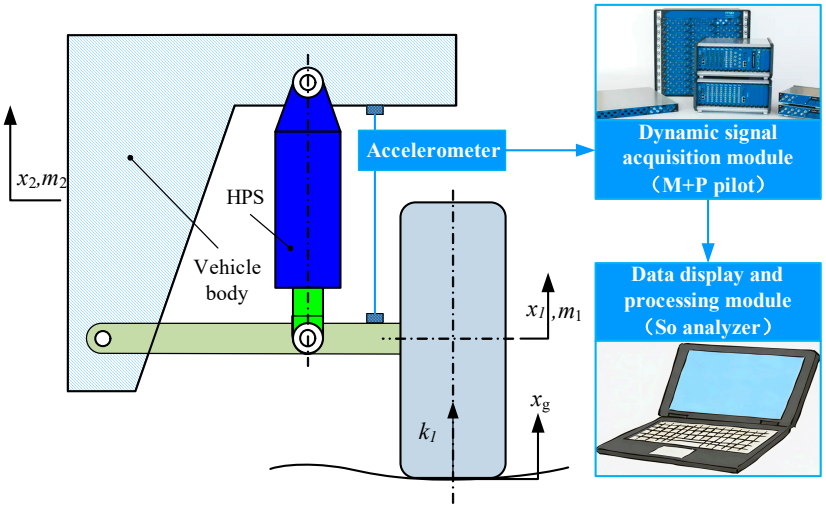



**Figure 7.** Vibration test scheme and its layout.

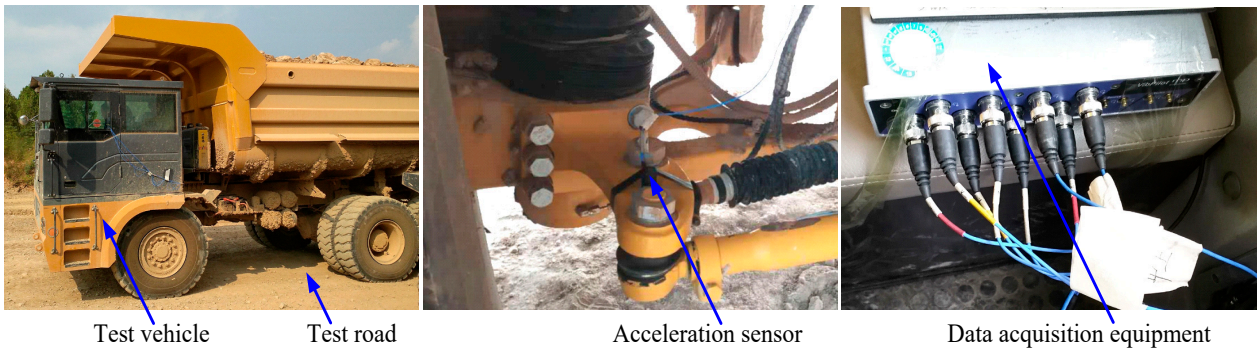



**Figure 8.** Vehicle and equipment for the experiment.

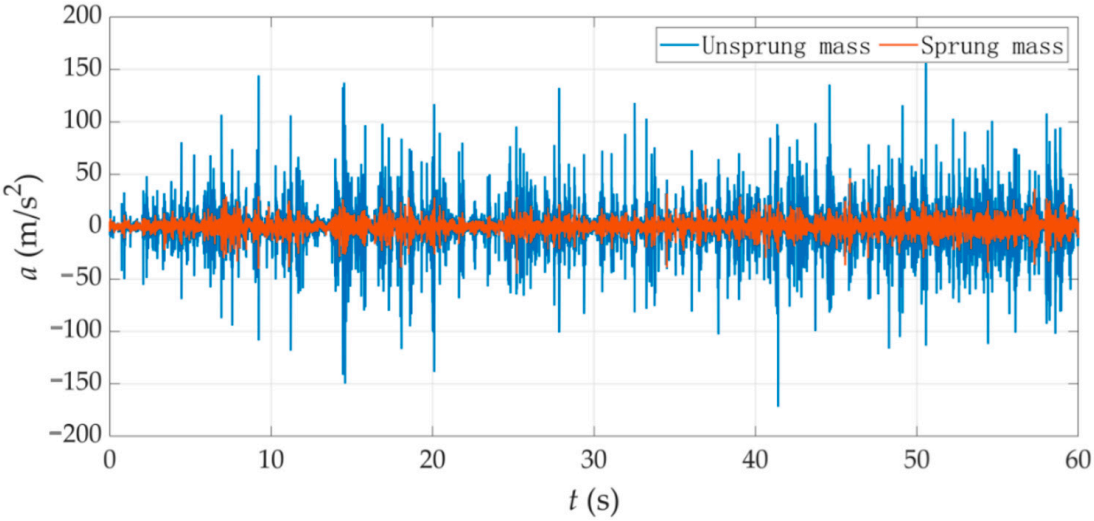



**Figure 9.** Measured time-domain acceleration responses of unsprung mass and sprung mass.

### *4.2. Wavelet Analysis Theory*

Wavelet analysis is a signal processing method developed based on the Fourier transform, which can characterize the local features of signals in both the time domain and the frequency domain [33–35]. Through wavelet analysis, the original signal can be decomposed into a series of sub-signals with different frequency ranges, specifically, as follows:

$$f(t) = a_n(t) + d_n(t) + d_{n-1}(t) + \ldots + d_2(t) + d_1(t) \tag{18}$$

where $f(t)$ is the original signal, $a$ is the low-frequency approximate part, $d$ is the high-frequency detailed part, and $n$ represents the number of decomposition layers.

The tree structure of signal decomposition using wavelet analysis is shown in Figure 10, which depicts a 3-layer decomposition process. In the figure, $F_s$ denotes the sampling frequency of the original signal. As can be seen from Figure 10, the low-frequency component in each layer decomposes the signal into two frequency bands, each occupying half of the bandwidth, while the high-frequency component is not decomposed. Therefore, for a given signal, an appropriate decomposition level can be determined to make the frequency components of interest fall into a specific frequency band. Meanwhile, the time-domain reconstructed signal within this frequency band can be easily obtained for further analysis.

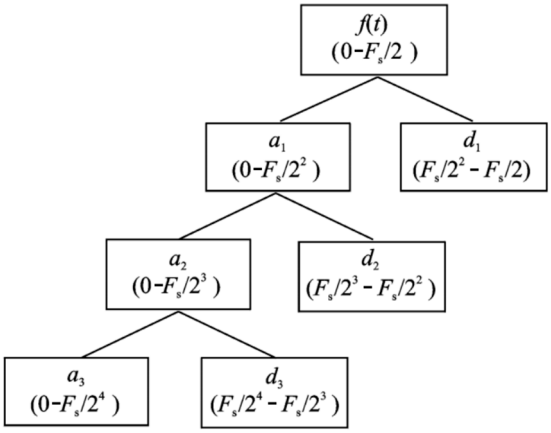



**Figure 10.** Wavelet decomposition and its frequency band division law.

### *4.3. Wavelet Data Processing*

The input of the vehicle model established in this paper only comes from road irregularity excitation. To ensure that the simulation results are as close as possible to the experimental results, combined with the wavelength of road irregularity and the vehicle driving speed, the test signals are filtered based on wavelet analysis to obtain the reconstructed time-domain signals within the frequency band of interest. In this study, the db4 wavelet basis (Daubechies 4 wavelet) is adopted. Characterized by compact support and moderate smoothness, it can effectively balance the resolution in both the time and frequency domains, making it suitable for feature extraction of non-stationary road vibration signals. It is a commonly used wavelet basis type in vehicle dynamics signal processing [33,34].

It is worth noting that according to the measured data of the Perryman area in the United States mentioned in reference [36], the spatial frequency range of unpaved roads is mainly between 0.011 and 1.6 $m^{-1}$. Given that the common speed range of mining dump trucks is [0, 60 km/h], the temporal frequency range of the road surface can be derived as [0, 26.7 Hz]. Combined with the sampling frequency of the road vibration signal (512 Hz), this study adopts the frequency bandwidth matching method to determine the number of decomposition layers. After 3-layer decomposition with the db4 wavelet, the low-frequency approximate component corresponds to the [0, 32 Hz] frequency band, which exactly and completely covers the target signal range [0, 26.7 Hz]. This approach can not only accurately extract the features related to road excitation, but also eliminate high-frequency noise interference. Meanwhile, three-layer decomposition can balance the adequacy of feature extraction and computational redundancy. If the number of decomposition layers is insufficient (e.g., 2 layers), the frequency band of the low-frequency component will be too wide ([0, 64 Hz]), leading to the mixing of irrelevant high-frequency noise. If the number of layers is excessive (e.g., 4 layers), the frequency band of the low-frequency component will be overly narrow ([0, 16 Hz]), which will result in the loss of key medium-high frequency components of road excitation and increase the risks of redundant computation and spurious features. Therefore, selecting 3-layer decomposition for signal reconstruction has clear rationality.

After reconstructing the low-frequency signal of the third layer via wavelet analysis, the time-domain signal within the range of [0, 32 Hz] is shown in Figure 11. Following the Fast Fourier Transform (FFT) of the acceleration, the PSD curve is shown in Figure 12, and the feature quantities of the reconstruction results are shown in Table 3.

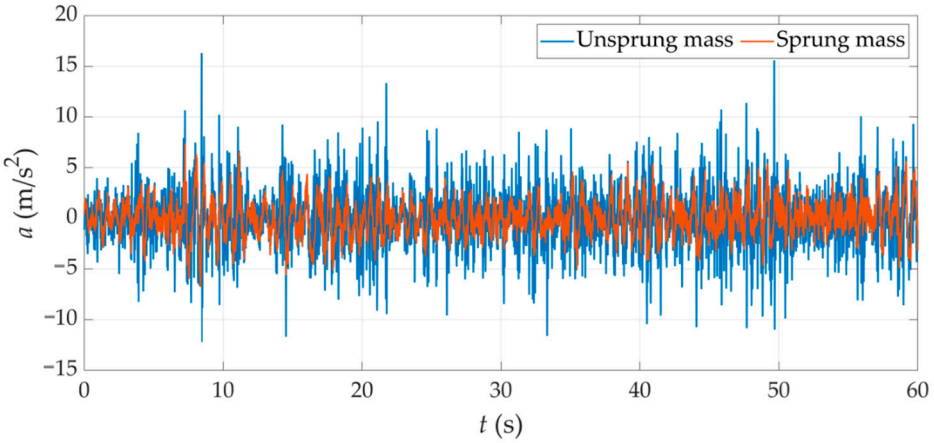



**Figure 11.** Measured time-domain acceleration responses of unsprung mass and sprung mass after wavelet reconstruction.

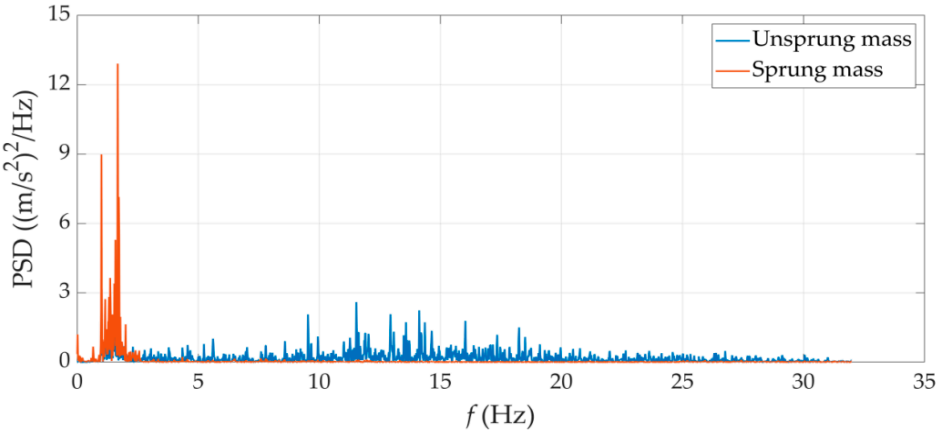



**Figure 12.** Measured frequency-domain acceleration responses of unsprung mass and sprung mass after wavelet reconstruction.

**Table 3.** Time–frequency domain feature quantities of experimental results after wavelet reconstruction.

| | | Unsprung Acceleration | Sprung Acceleration | Unit |
|---|---|---|---|---|
| Time Domain | Root Mean Square (RMS) | 2.57 | 1.76 | $m/s^2$ |
| | Min | −12.21 | −6.77 | $m/s^2$ |
| | Max | 16.31 | 7.38 | $m/s^2$ |
| Frequency Domain | Max PSD | 8.08 | 12.92 | $(m/s^2)^2/Hz$ |
| | Frequency at Max PSD | 1.67 | 1.67 | Hz |

## 5. Optimization Model for Road Spectrum Identification

Identifying the PSD of actual random road surfaces involves obtaining 3 parameters of random road surfaces, namely, $G_e$, $G_s$, and $G_a$. To reliably identify the parameters of the random road surface PSD, multiple feature quantities in the time—frequency domain of the response data are selected, with the optimization objective of minimizing the errors of these feature quantities to achieve the best approximation between simulation and experimental results. Based on the time—frequency domain feature quantities obtained from experiments, the following optimization model is constructed.

(1) Design Variables

$$X = [G_e, G_s, G_a]^T \tag{19}$$

(2) Objective Function

To ensure that the simulation system can fully reflect the experimental response results and render the identification outcomes more universally applicable, the objective function is designed to minimize multiple feature quantities in both the time domain and frequency domain between the simulation and experiment, forming a multi-objective optimization problem. For this purpose, corresponding weights are assigned to each feature quantity, and the established objective function is presented as follows:

$$\begin{aligned} f(X) = \omega_1\left(\frac{a_1^{\mathrm{rms}}-2.57}{2.57}\right)^2 + \omega_2\left(\frac{a_2^{\mathrm{rms}}-1.76}{1.76}\right)^2 + \omega_3\left(\frac{a_1^{min}+12.21}{12.21}\right)^2 + \\ \omega_4\left(\frac{a_1^{max}-16.31}{16.31}\right)^2 + \omega_5\left(\frac{a_2^{min}+6.77}{6.77}\right)^2 + \omega_6\left(\frac{a_2^{max}-7.38}{7.38}\right)^2 + \omega_7\left(\frac{f_1^{max}-1.67}{1.67}\right)^2 + \\ \omega_8\left(\frac{f_2^{max}-1.67}{1.67}\right)^2 + \omega_9\left(\frac{P_1^{max}-8.08}{8.08}\right)^2 + \omega_{10}\left(\frac{P_2^{max}-12.92}{12.92}\right)^2 \end{aligned} \tag{20}$$

where, $\boldsymbol{a_1^{\mathrm{rms}}}, \boldsymbol{a_2^{\mathrm{rms}}}, \boldsymbol{a_1^{min}}, \boldsymbol{a_1^{max}}, \boldsymbol{a_2^{min}}, \boldsymbol{a_2^{max}}, \boldsymbol{f_1^{max}}, \boldsymbol{f_2^{max}}, \boldsymbol{P_1^{max}}, \boldsymbol{P_2^{max}}$ denote the feature quantities obtained from the quarter-vehicle model simulation and corresponding data processing. Specifically, they are the RMS value of unsprung mass acceleration, the RMS value of sprung mass acceleration, the minimum value of unsprung mass acceleration, the maximum value of unsprung mass acceleration, the minimum value of sprung mass acceleration, the maximum value of sprung mass acceleration, the frequency corresponding to the maximum amplitude of the PSD of unsprung mass acceleration in the frequency domain, the frequency corresponding to the maximum amplitude of the PSD of sprung mass acceleration in the frequency domain, the maximum amplitude of the PSD of unsprung mass acceleration in the frequency domain, and the maximum amplitude of the PSD of sprung mass acceleration in the frequency domain. $\boldsymbol{\omega_1, \omega_2, \cdots, \omega_{10}}$ represent the weights of these feature quantities. Considering comprehensive factors, the values of the weight coefficients are set as shown in Table 4.

**Table 4.** Values of weight coefficients.

| $w_1$ | $w_2$ | $w_3$, $w_4$ | $w_5$, $w_6$ | $w_7$, $w_8$ | $w_9$, $w_{10}$ |
|---|---|---|---|---|---|
| 10 | 15 | 1 | 1 | 2 | 1 |

(3) Constraint Functions

The constraint functions mainly refer to boundary constraints. Based on the definitions and various road-specific values of $\boldsymbol{G_a}$, $\boldsymbol{G_s}$, and $\boldsymbol{G_e}$ provided in reference [30], and after careful consideration, the value ranges of the design variables are set as shown in Table 5.

**Table 5.** Value ranges of design variables.

| Design Variable | Symbol | Min | Max | Unit |
|---|---|---|---|---|
| $X_1$ | $Ga$ | 0 | 1 | $1/(\mathrm{m{\cdot}cycle}) \times 10^{-6}$ |
| $X_2$ | $Gs$ | 10 | 100 | $\mathrm{m/cycle} \times 10^{-6}$ |
| $X_3$ | $Ge$ | 0 | 1 | $\mathrm{m^3/cycle} \times 10^{-6}$ |

It should be noted that the selection of characteristic parameters and the setting of weight coefficients in this study are based on engineering experience and preliminary analysis. Although the results demonstrate that this method achieves favorable identification

performance under the current settings, the systematic optimization of feature and weight selection, along with the sensitivity analysis of their impacts on the results, constitutes a promising direction for future in-depth research, aiming to further enhance the adaptability and robustness of the method.

## 6. PSD Identification of Random Road Surfaces

When performing a Fourier transform on time-domain signals, their PSDs are affected by the sampling frequency and total sampling time. Therefore, to ensure the comparability of PSD between simulation and experimental results, the sampling frequency and total sampling time of the simulation are set to be the same as those of the experiment, i.e., 512 Hz and 60 s.

Surrogateopt belongs to the category of surrogate optimization, which is particularly suitable for optimization problems where each evaluation of the objective function requires significant time or computational resources. The fundamental idea of the algorithm is as follows: when directly optimizing the expensive real function $f(x)$ is infeasible, a computationally inexpensive surrogate model $s(x)$ is constructed to approximate it. Then, through an intelligent sampling strategy, the most promising points are iteratively selected to evaluate the real $f(x)$, and the new real data are used to update and improve the surrogate model, making it increasingly approximate the true function and, ultimately, guiding the search toward the optimal solution.

Surrogateopt can address the issue that traditional optimization algorithms, such as interior-point methods and SQP, require real-time gradient information [37]. Meanwhile, Surrogateopt leverages all information from the evaluation history to construct a statistical mathematical model. This overcomes the drawback of heuristic algorithms (e.g., particle swarm optimization, genetic algorithms) that fail to explicitly establish an approximate model of the entire problem space, leading to low search efficiency. Consequently, it can significantly enhance optimization efficiency [38].

In fact, each simulation result in this paper requires solving differential equations for 60 s, resulting in extremely high evaluation costs. Meanwhile, there is no direct mathematical relationship between the objective function constructed in this paper and the design variables. To address this, in order to improve optimization efficiency and achieve the best approximation of the actual road spectrum, the Surrogateopt algorithm is selected herein to solve the established optimization model.

To ensure the reproducibility of this study, the key implementation details of the surrogateopt algorithm are specified as follows: Latin hypercube sampling is adopted to generate initial samples (the number of samples is 10 times the variable dimension, i.e., 30 points), and a radial basis function surrogate model is constructed. In addition to a fixed number of iterations (200 times), the maximum number of function evaluations (500 times) and function value tolerance ($1 \times 10^{-4}$) are also set as stopping criteria. Each objective function evaluation (i.e., a single 60 s time-domain simulation) takes an average of approximately 12 s on the computing platform used (Intel Core i7-12700H, 32 GB RAM), and the completion of the entire optimization requires about 40 min. This demonstrates the efficiency advantage of the surrogate model method in addressing such high-cost simulation optimization problems.

The Surrogateopt algorithm is employed to solve the optimization model constructed in this paper, and the optimization iteration process is shown in Figure 13. After 200 optimization iterations, the minimum objective function value of 0.7660 is obtained. Table 6 presents the road spectrum identification results achieved by minimizing the feature quantity errors between simulation and experiment.

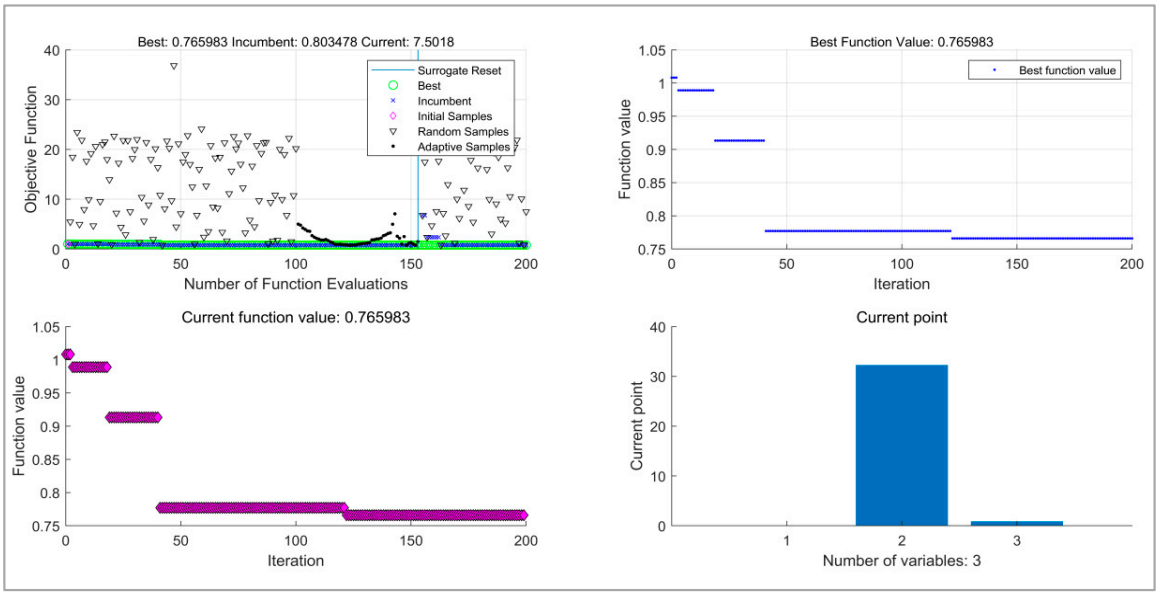



**Figure 13.** Optimization iteration process of the Surrogateopt algorithm.

**Table 6.** PSD identification results.

| Design Variable | Symbol | Identified Value | Unit |
|---|---|---|---|
| $X_1$ | $Ga$ | 0 | $1/(\mathrm{m}\cdot\mathrm{cycle}) \times 10^{-6}$ |
| $X_2$ | $Gs$ | 32 | $\mathrm{m}/\mathrm{cycle} \times 10^{-6}$ |
| $X_3$ | $Ge$ | 0.8819 | $\mathrm{m}^3/\mathrm{cycle} \times 10^{-6}$ |

## 7. Discussion on Road Spectrum Identification Results

Based on the random road spectrum parameters identified in Table 6, the time-domain curve of road irregularity is obtained using the IFFT method, as shown in Figure 14. Using this time-domain curve of road irregularity, a dynamic simulation of the quarter-vehicle model equipped with an HPS is performed. The simulation results of the unsprung and sprung mass accelerations are shown in Figures 15 and 16, respectively. The corresponding feature quantities and their errors relative to the experimental feature quantities are shown in Table 7.

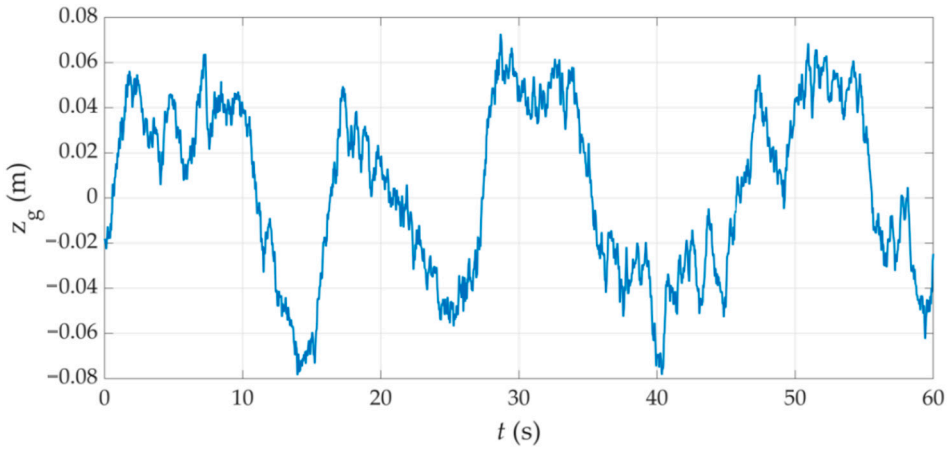



**Figure 14.** Time-domain curve of road irregularity for the identified road spectrum.

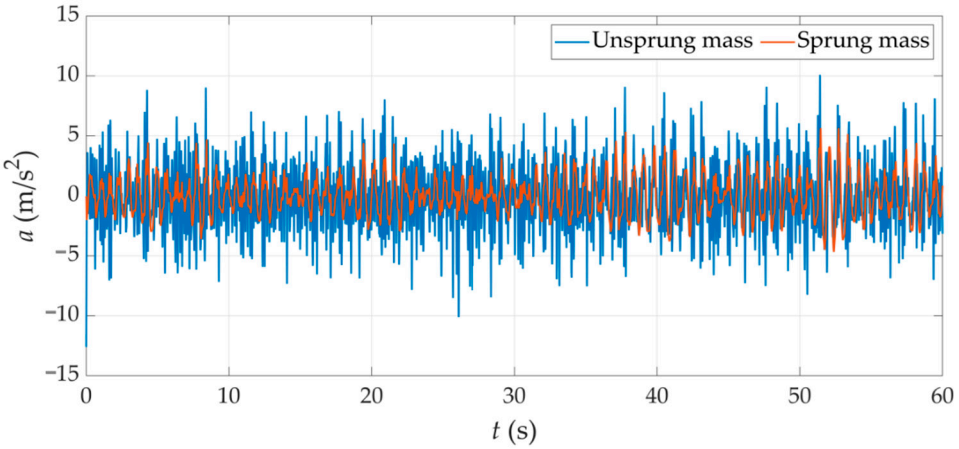



**Figure 15.** Time-domain responses of sprung and unsprung mass accelerations for the identified road spectrum.

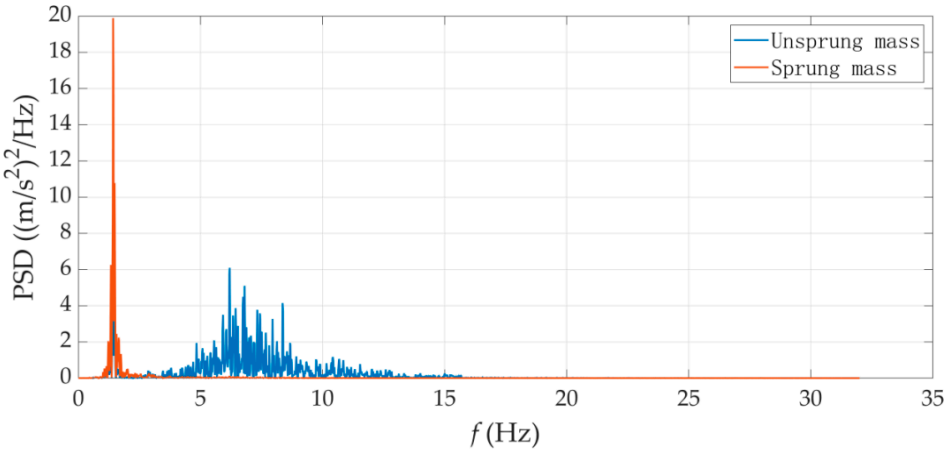



**Figure 16.** PSD responses of sprung and unsprung mass accelerations for the identified road spectrum.

**Table 7.** Time—frequency domain feature quantities and their errors between experimental and simulation results.

| | | | Experiment | Simulation | Unit | Relative Error |
|---|---|---|---|---|---|---|
| Time Domain | Unsprung | RMS | 2.57 | 2.60 | $m/s^2$ | 1.15% |
| | | Min | −12.21 | −12.61 | $m/s^2$ | 3.28% |
| | | Max | 16.31 | 10.09 | $m/s^2$ | −38.14% |
| | Sprung | RMS | 1.76 | 1.63 | $m/s^2$ | −7.39% |
| | | Min | −6.77 | −4.69 | $m/s^2$ | −30.72% |
| | | Max | 7.38 | 5.66 | $m/s^2$ | −23.31% |
| Frequency Domain | Unsprung | Max PSD | 8.08 | 7.37 | $(m/s^2)^2/Hz$ | −8.79% |
| | | Frequency at Max PSD | 1.67 | 1.42 | Hz | −14.97% |
| | Sprung | Max PSD | 12.92 | 19.89 | $(m/s^2)^2/Hz$ | 53.95% |
| | | Frequency at Max PSD | 1.67 | 1.42 | Hz | −14.97% |

### *7.1. Analysis of Identification Accuracy and Consistency*

The proposed road spectrum identification method exhibits good accuracy in key characteristic parameters. As can be seen from Table 7, the relative errors between the simulation and experiment results are small for the RMS values of the sprung and unsprung mass accelerations, which characterize the overall vibration energy (with values of −7.39%

and 1.15%, respectively). Meanwhile, the error of the characteristic frequency that reflects the dominant vibration mode of the system is −14.97%. The errors of these core parameters are all controlled within 15%, indicating that this method can effectively capture the main statistical characteristics of the actual road surface, and its identification results can provide more reliable inputs for vehicle dynamics simulation compared with traditional empirical classification methods.

The comparison between simulation and measured results also reveals certain discrepancies. The RMS value of sprung mass acceleration obtained from simulation is slightly lower than that from experiments. This may be attributed to the fact that the experimental signals still contain residual excitations from components such as the engine, and the roll and pitch motions of the actual vehicle are not represented in the quarter-car model. These factors together result in the generally lower simulated peak accelerations compared with the experimental values shown in Table 7.

It should be pointed out that there are relatively large errors in some transient characteristics (e.g., acceleration extreme values) and local frequency-domain amplitudes (e.g., Max PSD of sprung mass) presented in Table 7. These errors are mainly attributed to the following two reasons:

(1) Extreme values are susceptible to single large shocks or noise interference and feature high randomness, which are not the key parameters that this method aims to accurately reproduce.

(2) The deviation of PSD amplitude may reflect the discrepancy between the damping characteristics of the model and the actual situation. However, this method accurately identifies the dominant frequency, which is more crucial for the parameter inversion of road spectrum.

In summary, this method demonstrates favorable engineering applicability in identifying the parameters of road statistical characteristics, despite its limitations in reproducing all transient details.

### *7.2. Notes on Verification Scope and Universality*

The verification work of this study is based on the test data collected from a single road segment under the condition of a constant speed (20 km/h) with a single vehicle, which constitutes a limitation of the current conclusions. Although the proposed methodological framework is theoretically generic, its effectiveness and robustness across different vehicle types, various driving speeds, and a broader range of unpaved road types still await further verification and calibration through more comprehensive test data in future research.

### *7.3. Model Limitations and Future Research Directions*

The quarter-car model adopted in this study does not take into account the pitch and roll motions of the vehicle, as well as the excitation differences between the left and right wheels. Theoretically, this will introduce unquantified errors into the characterization of features such as acceleration extreme values and PSD peak values. At the current stage, this simplification is intended to focus on the principle verification of the feature fusion and inversion framework, and the consistency between simulation and experiment in terms of key characteristic parameters (see Table 7) indicates that its feasibility is acceptable.

Future research extensions should prioritize the establishment of a half-car or full-vehicle model incorporating pitch and roll degrees of freedom, so as to quantify the impacts caused by the current simplifications and improve the accuracy under complex working conditions. Further work can include integrating multi-sensor information, optimizing the cross-platform adaptability of algorithms, and developing real-time systems, thereby promoting the engineering application of this method in a broader range of scenarios.

## 8. Conclusions

Based on the establishment of a vehicle dynamic simulation model with nonlinear HPS and the collection of real-vehicle test data, this study organically integrates technologies such as IFFT-based road time-domain reconstruction, HPS system modeling, wavelet data processing, optimization model construction, and surrogate model optimization. This integration achieves accurate identification of the actual tested road spectrum, providing a fast and effective method for identifying unpaved road spectra.

This study comprehensively considers multiple time-frequency domain features of simulations and experiments, constructs a multi-objective optimization function for time-frequency domain feature errors, and employs an advanced surrogate optimization algorithm. The results show that the relative errors of several key features (root mean square values and feature frequencies) are all less than 15%, demonstrating reliable identification performance.

The proposed method does not rely on expensive direct measurement equipment. Instead, it can achieve fast and reliable identification of the corresponding road spectrum only by collecting data through conventional acceleration sensors and utilizing a suspension dynamic simulation model. This provides an engineering-practical road spectrum input scheme for the dynamic simulation and performance evaluation of mining vehicles operating on unpaved roads, featuring strong engineering applicability.

**Author Contributions:** Conceptualization, B.Q. and C.J.; methodology, B.Q. and C.J.; software, B.Q.; validation, B.Q. and C.J.; investigation, B.Q.; resources, B.Q. and C.J.; data curation, B.Q.; writing—original draft preparation, B.Q.; writing—reviewand editing, B.Q. and C.J.; formal analysis, B.Q.; supervision, C.J. All authors have read and agreed to the published version of the manuscript.

**Funding:** This research received no external funding.

**Data Availability Statement:** The original contributions presented in the study are included in the article, and further inquiries can be directed to the corresponding author.

**Conflicts of Interest:** The authors declare no conflicts of interest.

## References

1. Múčka, P.; Stein, G.J.; Tobolka, P. Whole-Body Vibration and Vertical Road Profile Displacement Power Spectral Density. *Veh. Syst. Dyn.* **2019**, *58*, 630–656. [CrossRef]
2. Hasegawa, S.; Kim, C.-W.; Chang, K.-C. Road Spectrum Identification by Means of Regularized Least Square Minimization with Dynamic Programming Utilizing Accelerations of a Moving Vehicle. *JJSCE A1* **2022**, *78*, 78–93. [CrossRef]
3. Huang, P.; Yao, Y.; Xiu, W.; Wu, J.; Geng, D.; Yang, Z.; Li, Y. Vibration Modelling and Testing of Off-Road Vehicle Incorporating Coupled Roll and Pitch Vibrations. *Biosyst. Eng.* **2024**, *240*, 111–122. [CrossRef]
4. Estanislau Dantas, A.; Correa de Faria, M.T. Off-Highway Truck Setup Influence on Vehicle Dynamics and Frame Durability. *Multibody Syst. Dyn.* **2024**, *65*, 417–439. [CrossRef]
5. Medvedev, M.V.; Pavlov, V.I. Road Surface Marking Recognition and Road Surface Quality Evaluation Using Convolution Neural Network. In *2020 International Multi-Conference on Industrial Engineering and Modern Technologies (FarEastCon)*; IEEE: New York, NY, USA, 2020; pp. 1–3. [CrossRef]
6. Russotto, S.; Migliore, M.; Orlando, S.; Pirrotta, A. A Low-Cost System for the Assessment of the Road Surface Quality. *Front. Built Environ.* **2025**, *11*, 1656913. [CrossRef]
7. Nguyen, T.; Lechner, B.; Wong, Y.D. Response-Based Methods to Measure Road Surface Irregularity: A State-of-the-Art Review. *Eur. Transp. Res. Rev.* **2019**, *11*, 43. [CrossRef]
8. Li, J.; Wang, L.; Miao, Y.; Tong, X.; Ye, Z. Road Roughness Detection Based on Discrete Kalman Filter Model with Driving Vibration Data Input. *Int. J. Pavement Res. Technol.* **2023**, *18*, 480–492. [CrossRef]
9. He, W.; Xi, J. A Quaternion Unscented Kalman Filter for Road Grade Estimation. In *2020 IEEE Intelligent Vehicles Symposium (IV)*; IEEE: New York, NY, USA, 2020; pp. 1635–1640. [CrossRef]
10. Huang, Z.; Fan, X.; Chen, M.; Peng, J. Joint Estimation Method of Sideslip Angle and Tyre–Road Adhesion Coefficient Using Extended Kalman Filter and Unscented Kalman Filter. *Veh. Syst. Dyn.* **2025**, 1–24. [CrossRef]

11. Pham, T.-P. Generalized H2 Observer for Road Profile Estimation in the Automotive Suspension System. *Heliyon* **2024**, *10*, e39928. [CrossRef]
12. Rabhi, A.; M'sirdi, N.K.; Fridman, L.; Delanne, Y. Second Order Sliding Mode Observer for Estimation of Road Profile. In *International Workshop on Variable Structure Systems, VSS'06*; IEEE: New York, NY, USA, 2006; pp. 161–165. [CrossRef]
13. Moon, J.; Park, W. Using Support Vector Machines to Classify Road Surface Conditions to Promote Safe Driving. *Sensors* **2024**, *24*, 4307. [CrossRef]
14. Dominic, H.; Patzer, M.; Harter, M. Automotive Radar Range Spectrum-Based Road Surface Classification by Using Machine Learning. *Sensors* **2025**, *25*, 6911. [CrossRef]
15. Han, Z.; Liu, W.; Gao, Z.; Liu, D. A Method for Real-Time Road Surface Identification of Intelligent Tire Systems Based on Random Convolutional Kernel Neural Network. *IEEE Trans. Intell. Veh.* **2024**, *9*, 6487–6501. [CrossRef]
16. Hsieh, C.-C.; Jia, H.-W.; Huang, W.-H.; Hsih, M.-H. Deep Learning-Based Road Pavement Inspection by Integrating Visual Information and IMU. *Information* **2024**, *15*, 239. [CrossRef]
17. Hadj-Attou, A.; Kabir, Y.; Ykhlef, F. Hybrid Deep Learning Models for Road Surface Condition Monitoring. *Measurement* **2023**, *220*, 113267. [CrossRef]
18. Van, C.N.; Tran, D.-N.; Long, T.T.; Thao, N.G.M.; Tran, D.-T. Hybrid Feature Selection for Real-Time Road Surface Classification on Low-End Hardware: A Machine Learning Approach. *Results Eng.* **2025**, *27*, 105693. [CrossRef]
19. Qin, Y.; Wang, Z.; Xiang, C.; Hashemi, E.; Khajepour, A.; Huang, Y. Speed Independent Road Classification Strategy Based on Vehicle Response: Theory and Experimental Validation. *Mech. Syst. Signal Process.* **2019**, *117*, 653–666. [CrossRef]
20. Kortiš, J.; Daniel, Ľ.; Holešová, M. Identification of the Moving Vehicle Presence on the Bridge with the Time-Frequency Analysis. *MATEC Web Conf.* **2017**, *107*, 00008. [CrossRef]
21. *ISO 2631-1:1997*; Mechanical Vibration and Shock—Evaluation of Human Exposure to Whole-Body Vibration—Part 1: General Requirements. International Organization for Standardization: Geneva, Switzerland, 1997.
22. Karpenko, M.; Prentkovskis, O.; Skačkauskas, P. Analysing the Impact of Electric Kick-Scooters on Drivers: Vibration and Frequency Transmission during the Ride on Different Types of Urban Pavements. *Eksploat. Niezawodn.—Maint. Reliab.* **2025**, *27*, 199893. [CrossRef]
23. Toshi, N.; Hasegawa, S.; Chang, K.C.; Kim, C.W. Vehicle Models for Road Profile Identification by Drive-by Bridge Inspection Method. In *Life-Cycle Civil Engineering: Innovation, Theory and Practice*; CRC Press: Boca Raton, FL, USA, 2021; pp. 320–327. [CrossRef]
24. Karpenko, M.; Prentkovskis, O.; Skačkauskas, P. Numerical Simulation of Vehicle Tyre under Various Load Conditions and Its Effect on Road Traffic Safety. *PROMTT* **2024**, *36*, 1–11. [CrossRef]
25. Jin, C.; Sun, H.L.; Zhang, W.M.; Li, H.; Tian, H.Y. Fractional Modeling and Characteristic Analysis of Hydro-pneumatic Suspension for Construction Vehicles. *Trans. Chin. Soc. Agric. Mach.* **2014**, *45*, 16–21. [CrossRef]
26. Liu, Y.S.; Xu, F.L.; Chen, Y.M. *Hydraulic and Pneumatic Transmission*, 5th ed.; China Machine Press: Beijing, China, 2024; pp. 20–29.
27. XU, H.L.; He, L.; An, D. The Simulation Realization of Pavement Roughness in the Time Domain. *IOP Conf. Ser. Earth Environ. Sci.* **2017**, *86*, 012016. [CrossRef]
28. Hu, Z.G.; Zhang, Y.L.; Ye, J.P.; Song, S.Y.; Chen, L.P. Numerical Modeling and Simulation of Random Road Surface Using IFFT Method. *AMR* **2011**, *199–200*, 999–1004. [CrossRef]
29. Lin, J.-H. Exploring the Relationship between the International Roughness Index (IRI) and the ISO 8608 Roughness Coefficient (Gd(n0)). *Int. J. Pavement Eng.* **2024**, *25*, 2359530. [CrossRef]
30. Gillespie, T.D.; Karamihas, S.M.; Sayers, M.W.; Nasim, M.A.; Hansen, W.; Ehsan, N.; Cebon, D. *Effects of Heavy-Vehicle Characteristics on Pavement Response and Performance (NCHRP Report No. 353)*; National Academy Press: Washington, DC, USA, 1993; pp. 111–118. Available online: https://www.researchgate.net/publication/30817762_ (accessed on 20 September 2025).
31. *GB/T 7031-2005*; Mechanical Vibration—Road Surface Profiles Reporting of Measured Data. Standards Press of China: Beijing, China, 2005.
32. Xie, Q.Q. New Concept Passenger Car Suspension Based on Hub Motor Drive Design. Master's Thesis, Shenyang Ligong University, Shenyang, China, 2024. [CrossRef]
33. Xin, X.; Jiao, Y.; Zhang, Y.; Liang, M.; Yao, Z. Research on Noise Reduction and Data Mining Techniques for Pavement Dynamic Response Signals. *SRT* **2024**, *6*, 115–129. [CrossRef]
34. Fu, X.; Zhao, Y. Machine Learning Road Recognition Based on Wavelet Decomposition. *J. Phys. Conf. Ser.* **2022**, *2301*, 012005. [CrossRef]
35. Alhasan, A.; White, D.J.; De Brabanterb, K. Continuous Wavelet Analysis of Pavement Profiles. *Autom. Constr.* **2016**, *63*, 134–143. [CrossRef]
36. Zhao, J.H.; Wang, Z.R.; Guan, C.L. *Measurement, Analysis and Application of Pavement Roughness*; Beijing Institute of Technology Press: Beijing, China, 2000; pp. 95–110.

37. Misener, R.; Biegler, L. Formulating Data-Driven Surrogate Models for Process Optimization. *Comput. Chem. Eng.* **2023**, *179*, 108411. [CrossRef]
38. Aivaliotis-Apostolopoulos, P.; Loukidis, D. Swarming Genetic Algorithm: A Nested Fully Coupled Hybrid of Genetic Algorithm and Particle Swarm Optimization. *PLoS ONE* **2022**, *17*, e0275094. [CrossRef]

**Disclaimer/Publisher's Note:** The statements, opinions and data contained in all publications are solely those of the individual author(s) and contributor(s) and not of MDPI and/or the editor(s). MDPI and/or the editor(s) disclaim responsibility for any injury to people or property resulting from any ideas, methods, instructions or products referred to in the content.